

Classical fully packed loop model with attractive interactions on the square lattice


Bhupen Dabholkar,^{1,*} Xiaoxue Ran,^{2,*} Junchen Rong,³ Zheng Yan,² G. J. Sreejith,⁴
Zi Yang Meng,^{2,†} and Fabien Alet^{1,‡}

¹*Laboratoire de Physique Théorique, Université de Toulouse, CNRS, UPS, France*

²*Department of Physics and HKU-UCAS Joint Institute of Theoretical and Computational Physics,
The University of Hong Kong, Pokfulam Road, Hong Kong SAR, China*

³*Institut des Hautes Études Scientifiques, 91440 Bures-sur-Yvette, France*

⁴*IISER Pune, Dr Homi Bhabha Road, Pune 411008, India*

 (Received 19 May 2023; revised 14 August 2023; accepted 22 August 2023; published 6 September 2023)

We study a classical model of fully packed loops on the square lattice, which interact through attractive loop segment interactions between opposite sides of plaquettes. This study is motivated by effective models of interacting quantum matter arising in frustrated magnets or Rydberg atom arrays, for which loop degrees of freedom appear at low energy. Through the combination of Monte Carlo simulations and of an effective height field theory, we find that the critical point known to occur at infinite temperature gives rise to a high-temperature critical phase with floating exponents. At lower temperature, the system transitions via a Kosterlitz-Thouless phase transition to a nematic phase where lattice rotation symmetry is broken. We discuss consequences for the phase diagram of the quantum loop model on the same lattice.

DOI: [10.1103/PhysRevB.108.125112](https://doi.org/10.1103/PhysRevB.108.125112)

I. INTRODUCTION

An important notion in the renormalization group theory is the emergence of effective degrees of freedom at low energies. These new degrees of freedom can have local structures which take the form of a *constraint*. For instance, for degrees of freedom that live on the bonds of a lattice, a gaugelike condition can emerge which requires that every site of the lattice is touched by a fixed number of occupied bonds. Related statistical mechanical models such as dimer or loop models arise as effective theories in many physical situations, such as in frustrated magnetic systems [1,2] as, e.g., in spin ice [3], Rydberg atom arrays [4–7], models of high- T_c superconductors [8], adsorption physics [9], quantum Hall effects [10,11], topological order [12], deconfined quantum critical points [13–22], etc. Loop models also have a long history in statistical physics [13,23–26], in relation to Potts models [27], Temperley-Lieb algebras [28], polymers and $O(N)$ models [29,30], Schramm-Loewner evolution [31], or percolation. These models often assign fixed fugacity for loops [23,24], but there are few results when the loop segments interact [32], even though loop interactions naturally arise in effective models of quantum condensed matter [8,33].

In this work, we study a two-dimensional (2D) classical statistical mechanical model of fully packed loops which attract locally. With the help of a directed-loop Monte Carlo algorithm [34–39] and a Coulomb gas [24] approach formulated in terms of a height-field description of the loop constraint [40,41], we obtain evidence for the existence

of a finite-temperature Kosterlitz-Thouless (KT) transition separating a high-temperature critical phase from a low-temperature nematic phase. Our results have similarities with those obtained for the classical dimer model with attractive interactions [35,42,43], albeit with specific differences that we highlight.

Aside from their interest in two-dimensional statistical mechanics in extending previous works on loop models [23–26,30,44], our results are also relevant for quantum-constrained models. First, the ground-state wave function at a Rokhsar-Kivelson point [8] (or its generalizations [45,46]) in the phase diagram of quantum loop models (QLM) maps to the partition function of a classical loop model. It is possible to construct extended quantum loop models (following the prescription in Ref. [45], see an example in Ref. [47] for a dimer model) whose ground-phase diagram is entirely given by the finite-temperature phase diagram of a classical (interacting) loop model, as the one we describe in this work. The second connection is made by realizing that the phase diagram of the classical model and the methods we use in its inference can serve to guide us in mapping out the finite-temperature phase diagram [48] and transitions of the quantum loop model [48–54] (see, e.g., the finite-temperature phase diagram of the quantum dimer model [55]). Such quantum-constrained models host a rich set of phases [7,48–54,56–61] and have recently been shown to be relevant in the context of Rydberg atom arrays [4,5,7,62–66], where the Rydberg blockade effectively implements the loop or dimer constraint.

The rest of the paper is organized as follows: In Sec. II, we introduce the classical loop model. Section III introduces the different physical observables computed in this work. Section IV provides a field theoretical perspective to the model and phase diagram in the form of a Coulomb gas analysis. The Monte Carlo simulation results and their analysis are

*These authors contributed equally to this work.

†zymeng@hku.hk

‡fabien.alet@cnrs.fr

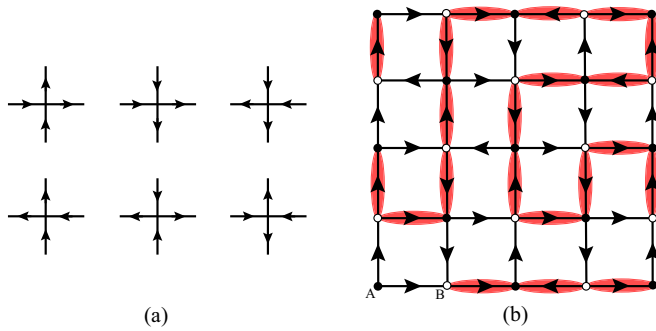


FIG. 1. (a) The allowed vertex types for the six-vertex model. (b) Correspondence between a six-vertex configuration and the fully packed loop configuration on the square lattice. The solid and open circles represent sites of the A and B sublattices, respectively. Placing dimers on all incoming arrows of the vertices on the A sublattice produces a fully packed loop configuration.

given in Sec. V, in which Sec. VA presents winding number fluctuations and Sec. VB an analysis of the low-temperature order parameter and its susceptibility. In Sec. VC, we discuss the behavior of various correlation functions in the high-temperature phase. These results are analyzed in light of the Coulomb gas predictions of Sec. IV. We present our conclusions and some perspectives in Sec. VI. Appendix A describes the Monte Carlo directed loop algorithm used in our numerical study and Appendix B contains further results on correlation functions.

II. MODEL AND METHODS

Configurations. Configurations of the fully packed loop model on a square lattice require two loop segments (or “dimers”) to touch each site of a square lattice, and are in one-to-one correspondence with configurations of the six-vertex model [67–72]. The ice-rule constraint of the six-vertex model associates an arrow on each bond and only allows vertices which have two arrows pointing inwards and two outwards from the lattice site. Under this constraint, there are six possible vertex configurations on the square lattice as shown in Fig. 1(a). The mapping from the six-vertex model to the loop model on the square lattice is illustrated in Fig. 1(b). If we place dimers on two incoming arrows on all sites of a sublattice of the square lattice, dimers will collectively form fully packed loops as every site is touched by exactly two dimers (“loop segments”).

Energetics. Loop or vertex models often associate a fugacity with each closed loop or to each type of vertex, respectively, to define the corresponding partition function [23]. The model that we study here associates an interaction energy term between proximate parallel loop segments, similar to the classical interacting dimer models [35,42]. We consider the following partition function and energy for an interacting fully packed loop model on the square lattice:

$$Z = \sum_c e^{-\beta E_c} \quad (1)$$

$$E_c = V(N(\text{□}) + N(\text{□})),$$

where the summation in the partition function Z is over all fully packed loop configurations on the square lattice and $\beta = 1/T$ is the inverse temperature. We assign an energy E_c to each covering in which $(N(\text{□}) + N(\text{□}))$ counts the number of plaquettes with parallel loop segments. Note that there is no energy assigned to a plaquette that has more than two loop segments. Here we set $V = -1$, which corresponds to *attractive* interactions between loop segments. We assume periodic boundary conditions for square lattices of linear size L with $N = L^2$ total number of sites. The model (1) is the limiting case of the quantum loop model on the square lattice [49] obtained when kinetic terms vanish in the QLM. To the best of our knowledge, this fully packed loop model with aligning interactions has never been studied earlier.

Limiting cases. The model admits two simple limits. At infinite temperature, it is equivalent to the six-vertex model at the ice point with equal fugacities for all vertices in Fig. 1(a) which is *critical* with power-law correlators (see the precise description below). At $T = 0$, there are two configurations which minimize the energy ($E_0 = -L^2$). These are *nematic* configurations with L horizontal or vertical loops that wrap around the boundary. The $\pi/2$ lattice rotation symmetry is broken at $T = 0$, and since this model admits only discrete energies (the first excited states have energies $E_1 = -L^2 + 4$) we expect a finite-temperature transition into a low-temperature nematic phase. As will be shown below, this transition is of Kosterlitz-Thouless (KT) type.

While the two limiting phases (critical and nematic) are easily identified, one cannot exclude other intervening phases. We will explore the finite-temperature phase diagram of the model using directed-loop Monte Carlo simulation [34–39], which allows for efficient nonlocal moves. The precise implementation we use is presented in Appendix A. The simulations are supplemented by a field-theoretical analysis in terms of a Coulomb gas description of the system (Sec. IV).

III. PHYSICAL OBSERVABLES

In this section, we describe the observables measured during the Monte Carlo simulations to characterize the phases and the transitions.

Winding number fluctuations. Fully packed loop configurations on the square lattice can be associated with two integer winding numbers W_x and W_y . To compute W_y (W_x), draw a horizontal (vertical) line that cuts across L lattice bonds oriented in the y (x) direction. For a given configuration, we denote by N_o and N_e the number of loop segments on the odd and even bonds that cross this line. The winding numbers are defined as $N_e - N_o$. Each winding number W_x and W_y vary between $-L$ and L , and there is at least one fully packed loop configuration for any pair (W_x, W_y) in this range. Note that the loop constraint ensures that the winding numbers calculated using different parallel lines are the same.

On account of translation symmetry, the equilibrium average values of W_x, W_y vanish, but not their fluctuations

$$\langle W^2 \rangle = \frac{1}{2} \langle W_x^2 + W_y^2 \rangle, \quad (2)$$

which have useful physical content and can easily be measured in Monte Carlo simulations [35,42,55,73,74].

configurations) and takes values $\bar{h} = \pm \frac{1}{4}$. v can also depend on temperature but its exact dependency is not relevant as long as it remains positive such that the two nematic configurations are always favored.

In the Coulomb gas language and given the periodicity of the height $h \rightarrow h + 1$ in the microscopic configurations, the latter vertex term can be identified with an electric charge $e = 2$ operator. This term is irrelevant at infinite temperature where $g = \frac{1}{3}$, but becomes relevant when $g \geq g_c = 1$ (a general electric charge e operator reads as $\exp(i2e\pi h)$, and has scaling dimension $e^2/(2g)$, and thus becomes relevant when $g \geq e^2/4$). As interactions favor the flat nematic phases, we expect g to increase [from its $g(T = \infty) = \frac{1}{3}$ value] as the temperature is lowered.

The Coulomb gas analysis predicts a Kosterlitz-Thouless phase transition [95–98] from a high-temperature critical phase to the low-temperature nematic phase, and furthermore provides predictions for several observables. First, the winding fluctuations can be related to the Coulomb gas constant [35]:

$$\langle W^2 \rangle = \sum_{n \in \mathbb{Z}} n^2 e^{-g\pi n^2} / \sum_{n \in \mathbb{Z}} e^{-g\pi n^2}, \quad (11)$$

as used in Fig. 2 below. This allows in particular to extract the Kosterlitz-Thouless transition temperature T_{KT} at the predicted critical Coulomb gas constant $g_c = 1$.

Next, the leading terms for the dimer and loop segment occupation operator *in the continuum* have been identified in Ref. [41] as

$$n_{\mathbf{-}}[\mathbf{r} = (x, y)] = \frac{1}{2} + (-)^{x+y+1} \nabla_y h - \frac{X}{2i} \{\exp[2i\pi h(\mathbf{r})] - \exp[-2i\pi h(\mathbf{r})]\}, \quad (12)$$

$$n_{\mathbf{+}}[\mathbf{r} = (x, y)] = \frac{1}{2} + (-)^{x+y} \nabla_x h + \frac{X}{2i} \{\exp[2i\pi h(\mathbf{r})] - \exp[-2i\pi h(\mathbf{r})]\}. \quad (13)$$

The loop-segment occupation is thus composed of a gradient part and a vertex part. The vertex part of the loop-segment operator can be expressed in harmonics of $2\pi h$ (as $h \equiv h + 1$) and microscopic $\pi/2$ rotations of the model give $h \rightarrow -h$ and $h \rightarrow h + \frac{1}{2}$. It can be identified with an electric charge $e = 1$ in the Coulomb gas.

Note that the overall sign in front of the gradient depends on the convention for the height (odd or even sublattice). The constant X cannot be fixed easily and we need an external exact solution (see below); in fact, we expect it to be renormalized, that is to change with temperature. This gives the following predictions for the leading terms of the correlators defined in Eqs. (5)–(7):

$$\begin{aligned} C^L[\mathbf{r} = (x, y)] &= \langle n_{\mathbf{-}}(0)n_{\mathbf{-}}(\mathbf{r}) \rangle - 1/4 \\ &= (-)^{x+y} A \frac{x^2 - y^2}{(x^2 + y^2)^2} + \frac{B}{(x^2 + y^2)^{1/2g}}, \end{aligned} \quad (14)$$

$$\begin{aligned} C^T[\mathbf{r} = (x, y)] &= \langle n_{\mathbf{+}}(0)n_{\mathbf{+}}(\mathbf{r}) \rangle - 1/4 \\ &= (-)^{x+y} A \frac{y^2 - x^2}{(x^2 + y^2)^2} + \frac{B}{(x^2 + y^2)^{1/2g}}, \end{aligned} \quad (15)$$

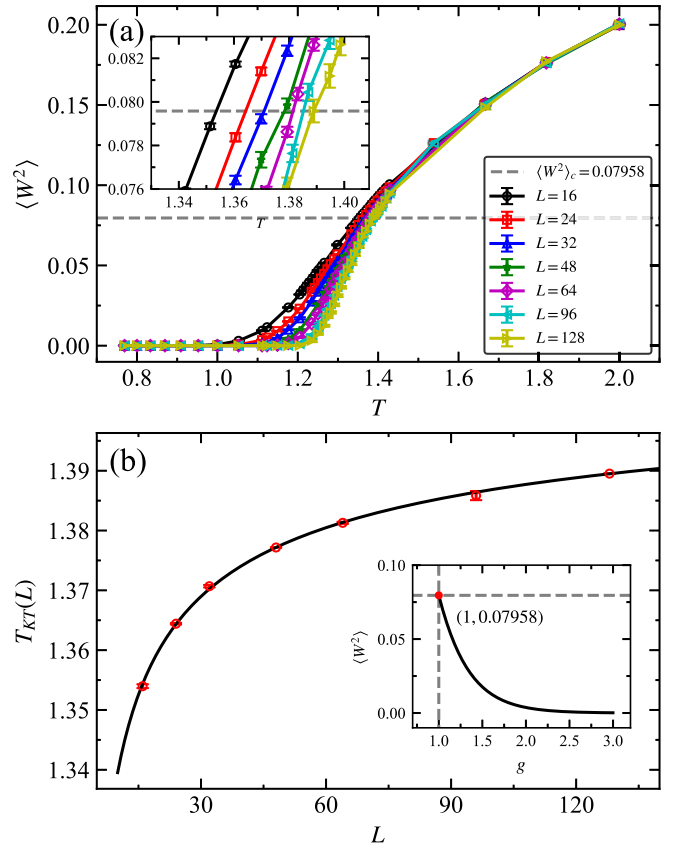


FIG. 2. (a) MC results for winding number fluctuations as a function of T . The gray dashed line shows the critical winding number fluctuations $\langle W^2 \rangle_c = 0.07958$, which is obtained from Eq. (11) with $g_c = 1$ at the transition point. Inset is a zoom-in for the $1.33 \leq T \leq 1.41$ region. (b) Finite-size scaling for the estimated transition temperature as a function of system size. The finite-size $T_{KT}(L)$ data points are obtained from (a). The black curve shows the fit to Eq. (18). The extrapolation to the thermodynamic limit gives $T_{KT} = 1.425(1)$. The inset shows $\langle W^2 \rangle$ as a function of g according to the relation in Eq. (11).

$$\begin{aligned} C^C[\mathbf{r} = (x, y)] &= \langle n_{\mathbf{-}}(0)n_{\mathbf{+}}(\mathbf{r}) \rangle - 1/4 \\ &= (-)^{x+y} A \frac{2xy}{(x^2 + y^2)^2} - \frac{B}{(x^2 + y^2)^{1/2g}}. \end{aligned} \quad (16)$$

The coefficient $A = \frac{1}{4g\pi^2}$ is fixed by the operator product expansion (12) and the two-point correlation function $\langle h(x)h(y) \rangle$ known exactly for free compact boson conformal field theory [99]. We also have $B = X^2/2$, however, its dependence on g is not universal. At $T = \infty$, exact expressions for the XXZ spin chain [94] give $B \simeq 0.01795$ (see Table 1 in Ref. [94]) (see also Ref. [82]).

Finally, we note that on the lattice, a monomer creates a dislocation of ± 1 in the height field. The prediction of the monomer correlator decaying as

$$M(r) \propto r^{-g} \quad (17)$$

follows [35,43] from the identification of the monomer operator with the $m = \pm 1$ magnetic charge operator (the sign

depends on the sublattice) with a scaling dimension $gm^2/2$.

This interpretation parallels the one for the interacting classical dimer model [35,42,43] with the following three minor (albeit important for numerics) distinctions: (i) The infinite-temperature value of the Coulomb gas constant $g = \frac{1}{3}$ renders the vertex contribution (scaling as r^{-3}) *subleading* with respect to the dipolar contribution (scaling as r^{-2}), which explains why it is often not reported in the polarization fluctuations for the six-vertex model [80]. For the dimer problem, we have $g(T = \infty) = \frac{1}{2}$ and both terms contribute equally to the r^{-2} decay of the dimer correlators [82]. (ii) The critical value of the Coulomb gas constant at the critical point is $g_c = 1$ (instead of $g_c = 4$ for the dimer model), consistent with the lower degeneracy of the ground states (2 nematic ground states instead of 4 columnar ground states for the dimer model) and resulting in a larger value of the anomalous dimension of the low-temperature order parameter $\eta_D = 1/g_c = 1$ for the loop model (see below) instead of $\eta_D = 1/g_c = \frac{1}{4}$ for the dimer model at their respective KT transitions [42]. (iii) Lastly, we found the critical value for the winding fluctuations $\langle W^2 \rangle$ is much *larger* for the loop model, which allows for a statistically meaningful measurement in the Monte Carlo simulations. The very small value of $\langle W^2 \rangle$ for the dimer model does not allow for an accurate Monte Carlo determination of the critical point using the value of the winding number fluctuations.

V. MC SIMULATION RESULTS

We present our Monte Carlo (MC) simulation results in this section. It contains results for observables from which we can precisely estimate the critical temperature T_{KT} : the winding number fluctuations (Sec. V A) and the essential singularity of the nematic susceptibility in the KT transition (Sec. V B). Section V C presents results for different correlation functions in the high-temperature critical phase, confirming the field-theoretical analysis presented in Sec. IV.

A. Winding number fluctuations

The numerical results for the winding number fluctuations $\langle W^2 \rangle$ as a function of temperature T of the classical loop model are shown in Fig. 2(a). We simulate system sizes up to $L = 128$ for this measurement. These data directly provide the temperature dependence (albeit on finite size) of the Coulomb gas constant, which will later be compared with other estimates of $g(T)$. At the transition point, the analysis of Sec. IV predicts the critical Coulomb gas constant g_c to be 1, corresponding to the critical winding number fluctuations $\langle W^2 \rangle_c = 0.07958$ [from Eq. (11), also see inset of Fig. 2(b)]. The predicted critical value $\langle W^2 \rangle_c$ is shown as the gray dashed horizontal line in Fig. 2(a) and in its inset.

We estimate the transition temperature $T_{KT}(L)$ for each system size as the temperature at which the winding number fluctuations cross the critical value, which is in turn estimated from a linear fit of the data points near $\langle W^2 \rangle_c$ [Fig. 2(a) inset] This estimate has an obvious finite-size dependence. To determine the transition temperature T_{KT} in the thermodynamic limit, we use the following finite-size scaling relation for a KT

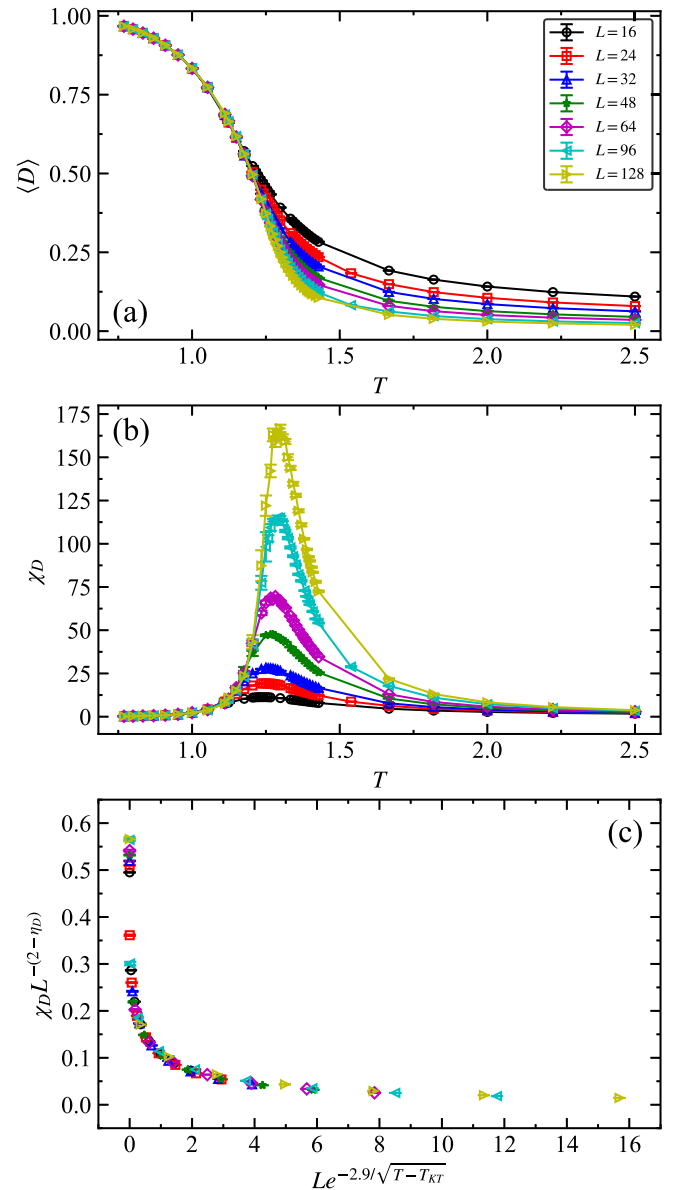


FIG. 3. (a) The nematic order parameter $\langle D \rangle$ as a function of temperature for different system sizes. (b) Susceptibility χ_D of the nematic order parameter defined in Eq. (4). Data collapse is performed in (c) the critical phase with $T > T_{KT}$. Here we use $\eta_D = 1$ and $T_{KT} = 1.425$, and all the data points nicely collapse onto a single curve.

transition [92,100,101]:

$$\frac{1}{T_{KT}(L)} = \frac{1}{T_{KT}} + \frac{C}{\log(L/L_0)^2}, \quad (18)$$

where C is a constant. By fitting the estimated $T_{KT}(L)$ in Fig. 2(b) with Eq. (18), we obtain $T_{KT} = 1.425(1)$.

B. Nematic order parameter and susceptibility

Our results for the finite-temperature behavior of the nematic order parameter $\langle D \rangle$ defined in Eq. (3) are presented in Fig. 3(a) for different system sizes. We clearly observe the existence of a nematic phase at low temperature, where

$\langle D \rangle$ takes a finite value, and a high-temperature phase where $\langle D \rangle$ vanishes relatively slowly as system sizes increase. The associated nematic susceptibility χ_D [Eq. (4)], represented in Fig. 3(b), shows a clear diverging peak (with system size) in the temperature range where $\langle D \rangle$ starts to vanish.

There is a clear shift in the temperature of the peak in χ_D as system size varies, as this can be used to perform a data collapse in order to cross validate the transition temperature T_{KT} obtained in the previous section. In the vicinity of the KT transition, we indeed expect that the susceptibility χ_D obeys the scaling behavior [98]

$$\chi_D \sim L^{2-\eta_D} f \left[L \exp \left(-\frac{K}{\sqrt{T-T_{KT}}} \right) \right] \quad (19)$$

for $T > T_{KT}$ where K is a constant and $\eta_D = 1/g_c = 1$ the anomalous dimension [42]. Such data collapse has been used in the literature to determine the Kosterlitz-Thouless transition temperature T_{KT} in many 2D systems such as the 2D XY model [100], magnetic thin films [101], triangular lattice transverse field Ising model [102], or for the pairing transition in various 2D fermionic lattice models [76–79]. We use the data in the $T > T_{KT}$ region to rescale the y axis as $\chi_D L^{-(2-\eta_D)}$ and the x axis as $L \exp(-\frac{K}{\sqrt{T-T_{KT}}})$ as shown in Fig. 3(c). We obtain that values $T_{KT} = 1.425$, $\eta_D = 1$ provide a good data collapse, resulting in a good agreement with the T_{KT} obtained in Fig. 2(b).

C. Correlation functions

The height description of the loop-segment correlations given in Eqs. (14), (15), and (16) suggests that the correlators have two contributions: from the vertex and the dipolar part [36,41,82,94]. We show the correlators calculated from the Monte Carlo methods for $L = 256$ system and present the fits to their expected forms in Appendix B. Below we present a simpler approach to fitting by considering combinations of the correlators that separate out the vertex and dipolar terms.

We first consider the sum $C^L + C^T = \langle n_{\mathbf{0}}(0)n_{\mathbf{r}} \rangle + \langle n_{\mathbf{0}}(0)n_{\mathbf{r}} \rangle - \frac{1}{2}$ which should contain only a vertex contribution $2B/(x^2 + y^2)^{1/2g}$. This combination for the direction $\mathbf{r} = (r, 0)$ is shown in Figs. 4(a) and 4(b) in linear and logarithm scales, respectively. Consistent with the expected form, the combination shows a power-law scaling with distance r with an exponent (slope in the logarithm plot) that increases with temperature. The estimated value of g from this combination is discussed further below.

We then consider the crossed correlators $C^C = \langle n_{\mathbf{0}}(0)n_{\mathbf{r}} \rangle - \frac{1}{2}$ along the direction $\mathbf{r} \equiv (r, 0)$, where the correlation is expected to be dominated by the vertex term according to Eq. (16). Monte Carlo estimates of $C^C(r)$ for different temperatures are shown in Fig. 4(c). The crossed correlators show expected power-law scaling at large distances but with a possible oscillatory subleading correction that affects the short-distance correlations, which is visible at higher temperatures. We tentatively attribute this effect to further subleading terms that do not cancel for $y = 0$ and are not included in Eq. (16). This is confirmed by a fit to the form $(-1)^r A'/r^{\alpha_S} + B'/r^{\alpha_U} + C$ for $C^C(r)$ in Fig. 4(c), where we find that the amplitude A' of the oscillating term is always small, and almost vanishing as the temperature lowers

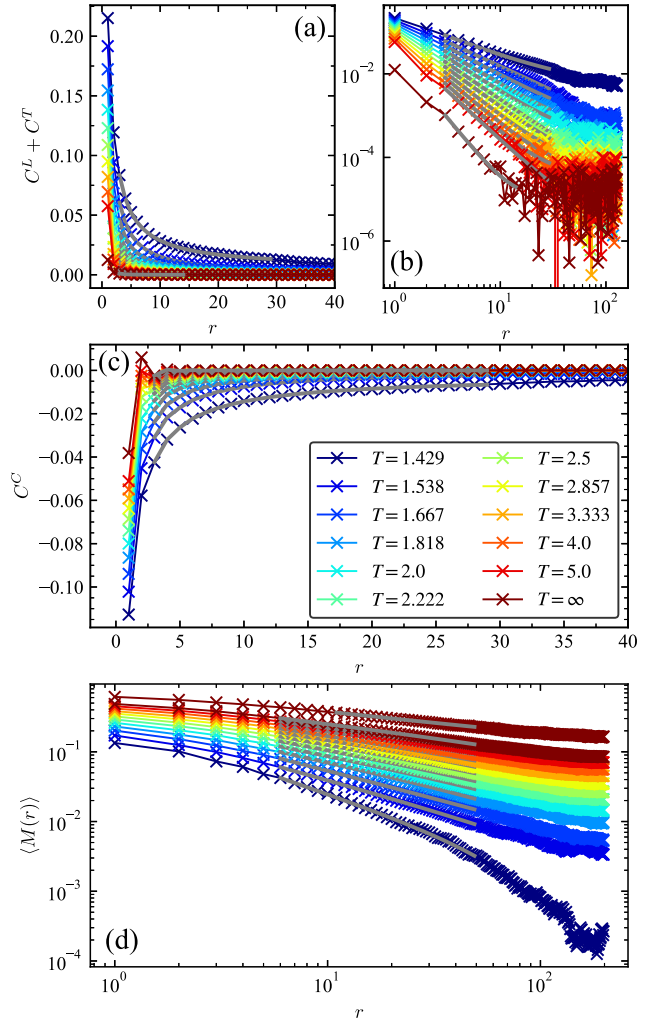


FIG. 4. Equal-time loop-segment correlation functions (a) $C^L + C^T$ as a function of r , (b) the log-log plot for $|C^L + C^T|$ (absolute value is used to correct for very small negative values occurring at large r , large T due to statistical fluctuations caused by the finite Monte Carlo sampling). (c) The crossed correlations C^C [Eq. (7)], and (d) the log-log plot of the monomer correlations $\langle M(r) \rangle$ in Eq. (9). The system size is $L = 256$ for the loop-segment correlators and $L = 400$ for monomer correlations. These data correspond to the high-temperature critical phase, that is, temperatures above the estimated $T_{KT} = 1.425$. Gray curves are power-law fits (in their respective fitting range) according to the scaling form $B'/r^{1/g} + C$ for $C^L + C^T$, $(-1)^r A'/r^{\alpha_S} + B'/r^{\alpha_U} + C$ for C^C , and $B'/r^g + C$ for $M(r)$. In all cases, we add a constant to the power-law fits to account for a small nonvanishing value of correlators at large distance in our finite-size Monte Carlo simulations.

towards the critical point (e.g., $A' \sim 0.03$ for $T = 4$ and $A' \sim 0.002$ for $T = 1.3$). The results of this fit for α_U allow to estimate g as obtained from Eq. (16) and as presented below.

Next, we study the combination $C^L - C^T = \langle n_{\mathbf{0}}(0)n_{\mathbf{r}} \rangle - \langle n_{\mathbf{0}}(0)n_{\mathbf{r}} \rangle$ which, based on Eqs. (14) and (15), is expected to have a purely staggered dipolar contribution $(-)^r/r^2$. Our results for $(-)^r(C^L - C^T)(\mathbf{r})$ in the $\mathbf{r} = (r, 0)$ direction are presented in Fig. 5(a). We observe

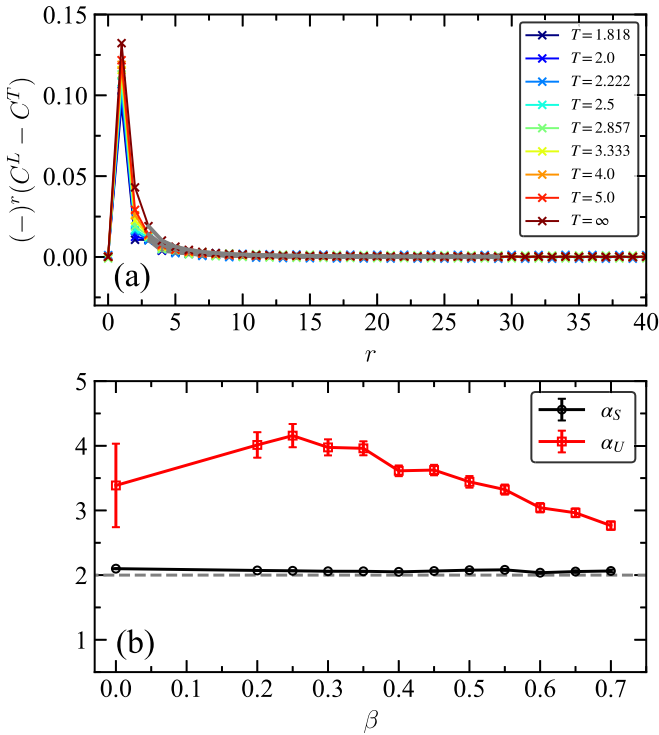


FIG. 5. (a) The equal-time loop-segment correlation functions of $(-)^r(C^L - C^T)$ for $L = 256$. A weak staggered part can be observed in this representation (particularly visible for the lowest temperatures at short distances), signaling a small uniform component for $(C^L - C^T)$. The gray curves fit $(C^L - C^T)$ to the form $(-1)^r A' / r^{\alpha_S} + B' / r^{\alpha_U} + C$. (b) The two exponents α_S and α_U obtained from this fit.

that there is a small but nonvanishing uniform component in the numerical data [which appears as a staggered part in Fig. 5(a) due to the $(-)^r$ factor]. To account for this, we fit $C^L - C^T$ to a form $(-1)^r A' / r^{\alpha_S} + B' / r^{\alpha_U} + C$. The constant C accounts for a nonzero value of this correlator present only at temperatures close to the phase transition, which we attribute to the finite sizes used in our Monte Carlo simulations. Here α_U is meant to describe a subleading correction to the vertex part not included in Eqs. (14) and (15). The estimates for α_S, α_U are presented in Fig. 5(b), where we find that α_S is very close to the predicted value 2 all along the high-temperature critical phase, and $\alpha_U > \alpha_S$ confirming the subleading nature of this uniform correction. If we fit the data fixing α_U to be zero, the exponent α_S is always larger than its expected value of 2.

Finally, the monomer-monomer correlator $M(r)$ in Eq. (9) should decay only with the vertex contribution $1/r^8$ [36,42,55,103]. We present the monomer correlations $M(r)$ at different temperatures in Fig. 4(d) for $L = 400$ [within the directed loop algorithm, we can get good statistics for $M(r)$ for larger systems than for loop-segment correlators]. The log-log plot shows a clear power-law decay above the Kosterlitz-Thouless transition temperature.

We now collect, in Fig. 6, the estimates of the Coulomb gas constant obtained from the fits to the correlators $C^L + C^T$ [from Figs. 4(a) and 4(b)], C^C [from Fig. 4(c)] and $M(r)$ [from Fig. 4(d)] as well as from the winding number fluctuations $\langle W^2 \rangle$ in Fig. 2. Figure 6 shows the temperature dependence

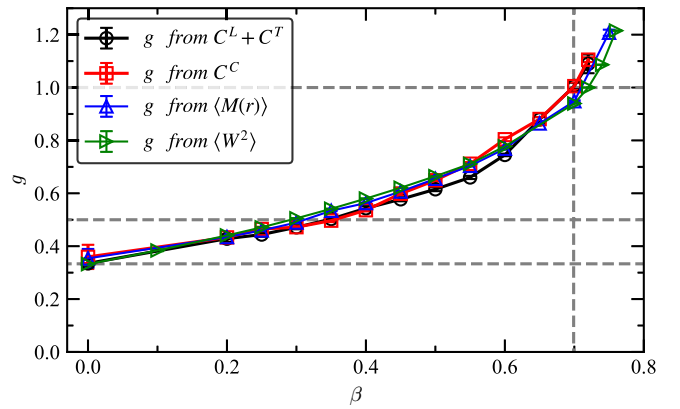


FIG. 6. The Coulomb gas constant g obtained from Figs. 4(b)–4(d), and $\langle W^2 \rangle$. The vertical gray dashed line indicates the transition point $\beta_{KT} = 1/T_{KT} \simeq 0.7$. The upper gray dashed line in the horizontal direction denotes the critical value $g_c = 1$; the middle one at $g = \frac{1}{2}$ corresponds to the case where the vertex and dipolar terms have the same contribution to scaling, the lowest gray dashed lines indicate the infinite-temperature value $g = \frac{1}{3}$.

of g as a function of inverse temperature $\beta = 1/T$. We find that as β increases (i.e., as the temperature decreases), the Coulomb gas constant increases from its infinite-temperature value $\frac{1}{3}$, which is consistent with the expectation that attractive interactions tend to *stiffen* the loops. As the temperature decreases from the $T = \infty$ point to finite but high temperature, the dipolar part in Eqs. (14), (15), and (16) dominates down to a temperature $T \approx 3$, below which $g > \frac{1}{2}$ and the vertex part takes over down to $T_{KT} \simeq 1.425$ ($\beta_{KT} \simeq 0.7$) where $g = 1$. The various estimates of g are overall in good agreement (we note the g value obtained from C^C is less accurate due to the subleading oscillations at high temperature) with each other, and consistent with the theoretical expectations of Sec. IV.

VI. DISCUSSION AND CONCLUSIONS

In this work, we investigated the finite-temperature phase diagram of a classical model of fully packed loops on the square lattice with attractive local interactions between loop segments. With the help of a directed-loop Monte Carlo algorithm and a field-theoretical analysis based on a height description of loop configurations, we are able to locate the finite-temperature Kosterlitz-Thouless transition, separating a critical phase at $T > T_{KT}$ and a nematic phase below T_{KT} . We find that in the loop model the anomalous dimension at the KT transition $\eta_D = 1$ is four times larger than that in the classical dimer model [42]. The high-temperature critical phase is fully characterized by the temperature dependence of the Coulomb gas constant presented in Fig. 6, which is obtained using several different concurrent estimates.

An interesting, closely related system to consider would be a similar classical model, but with *repulsive* interactions ($V > 0$) between fully packed loops, favoring large-winding sectors. Analogous repulsive interactions in the dimer model result in a continuous phase transition from a critical to staggered phase, which has been argued to be in the two-dimensional Ising universality class [92].

We connect our results to the quantum loop model on the square lattice. From our analysis, we expect that the QLM on the square lattice should also host a critical phase at any sufficiently high-temperature parametrized by a Coulomb gas constant $g(T/t, V/t)$ which depends on temperature and potential energy, similar to the quantum dimer model [55]. In general, a high-temperature critical phase can be found in the constrained entropic scaling regime of several strongly constrained quantum systems, which can extend down to low temperatures (see Ref. [104] for an extensive discussion). At large negative ratio of potential to kinetic energy ($V/t \ll 0$), the QLM hosts a nematic ground state. From our results, we conclude that the finite-temperature phase transition to the nematic phase in the QLM should occur as a Kosterlitz-phase transition that can be described using the same analysis provided here. The QLM also hosts a plaquette ground state in a finite range of $-0.35 \lesssim V/t \ll 1$ [53]. We believe that the finite-temperature phase transition to this plaquette phase should be of KT type too, with an effective action described by Eq. (10) but with *negative* v , as the two plaquette ground states have average height $\bar{h} = 0, \frac{1}{2}$. It would be interesting to find a classical model with a similar phase transition and low-temperature phase. Finally, we note that the directed loop algorithm that we use can be directly implemented as a new move [55] within the sweeping cluster algorithm [105,106] for the QLM, allowing the study of its finite-temperature phase diagram fully taking into account the loop constraints and winding fluctuations.

Rydberg atom arrays form a new type of platform where constraints (due to the Rydberg blockade) play an important role to determine the ground-state phase diagram, with a rich variety of phases observed [5,7,62,64,65,107]. To the best of our knowledge, the finite-temperature phase transitions out of these phases has not been studied experimentally so far. It would be interesting to see where the finite-temperature critical phase that we find here could be relevant in some experimental regimes where the fully packed constraint is a relevant approximation in Rydberg atom arrays.

ACKNOWLEDGMENTS

We acknowledge support from the ANR/RGC Joint Research Scheme sponsored by Research Grants Council of Hong Kong SAR of China (Project No. A_HKU703/22) and French National Research Agency (Grant No. ANR-22-CE30-0042-01). X.X.R., Z.Y., and Z.Y.M. further acknowledge the support from the Research Grants Council of Hong Kong SAR of China (Projects No. 17301420, No. 17301721, No. AoE/P-701/20, No. 17309822, No. HKU C7037-22G), and B.D., G.J.S., and F.A. the support from the joint PhD program between CNRS and IISER Pune, as well as the Grant No. NanoX ANR-17-EURE-0009 in the framework of the French “Programme des Investissements d’Avenir”. The research of J.R. is supported by the Huawei Young Talents Program at IHES. We acknowledge the use of high-performance computing resources from CALMIP (Grants No. 2022-P0677 and No. 2023-P0677), GENCI (Projects No. A0110500225 and No. A0130500225), the HPC2021 system under the Information Technology Services, the Blackbody HPC system at the Department of Physics, University of Hong Kong and Param Brahma

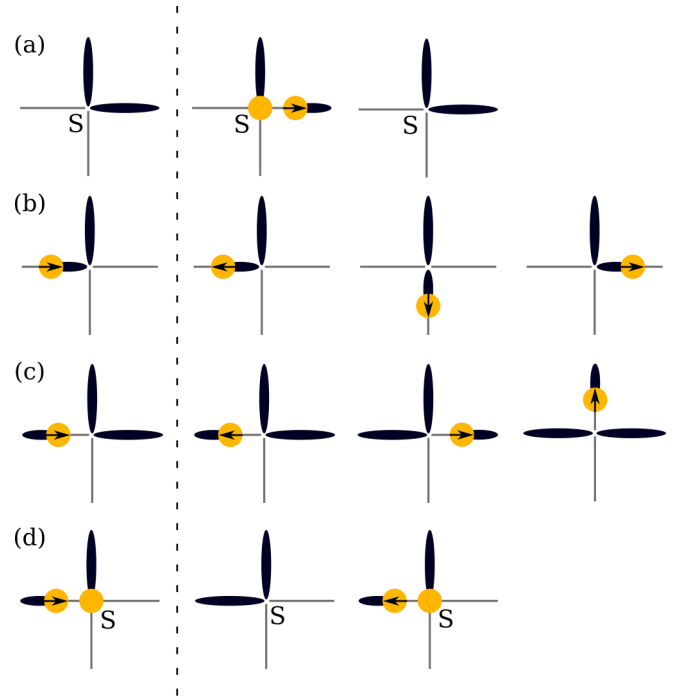


FIG. 7. Directed-loop Monte Carlo update steps for the fully packed loop model. The local configuration to the left of the dotted line can transition into one of the configurations to its right with probabilities determined by detailed balance.

computing facility at IISER Pune. G.J.S. and B.D. thank K. Damle for useful discussions as well as TIFR, Mumbai, for hospitality during the completion of this work.

APPENDIX A: DIRECTED-LOOP ALGORITHM FOR LOOP MODELS

We estimate the thermal averages of observables in the classical loop model as averages over Monte Carlo samples generated by a directed loop algorithm [34–39] tailored for the loop model. The algorithm is summarized below.

(1) Given a fully packed loop configuration \mathcal{C} , we pick with uniform probability a site S ; and then choose one of the two occupied edges around S . With a Metropolis probability $p_0 = \min(1, e^{\beta[E(\mathcal{C}) - E(\mathcal{C}')]})$, the dimer on this edge is replaced by half a dimer [Fig. 7(a)]. The new configuration \mathcal{C}' has monomers on the site S and at the end (monomer M) of the dimer. The monomer M has a binary valued “momentum” internal degree of freedom that is, initially, directed into the dimer and away from S . In calculating the configurations E , it is assumed that the interaction between half-dimers and parallel dimers is half that of full dimers. Note that parallel dimers in a plaquette interact only if the other two edges are empty. With probability $1 - p_0$ the move is abandoned in this first step itself.

(2) If the monomer M is moving into a dimer, annihilating it in the process [Fig. 7(b)], it can, subsequently, create a dimer on one of the two previously empty edges connected to the site ahead or the monomer can just reverse its direction. Transition probabilities are chosen to satisfy detailed balance as described further below.

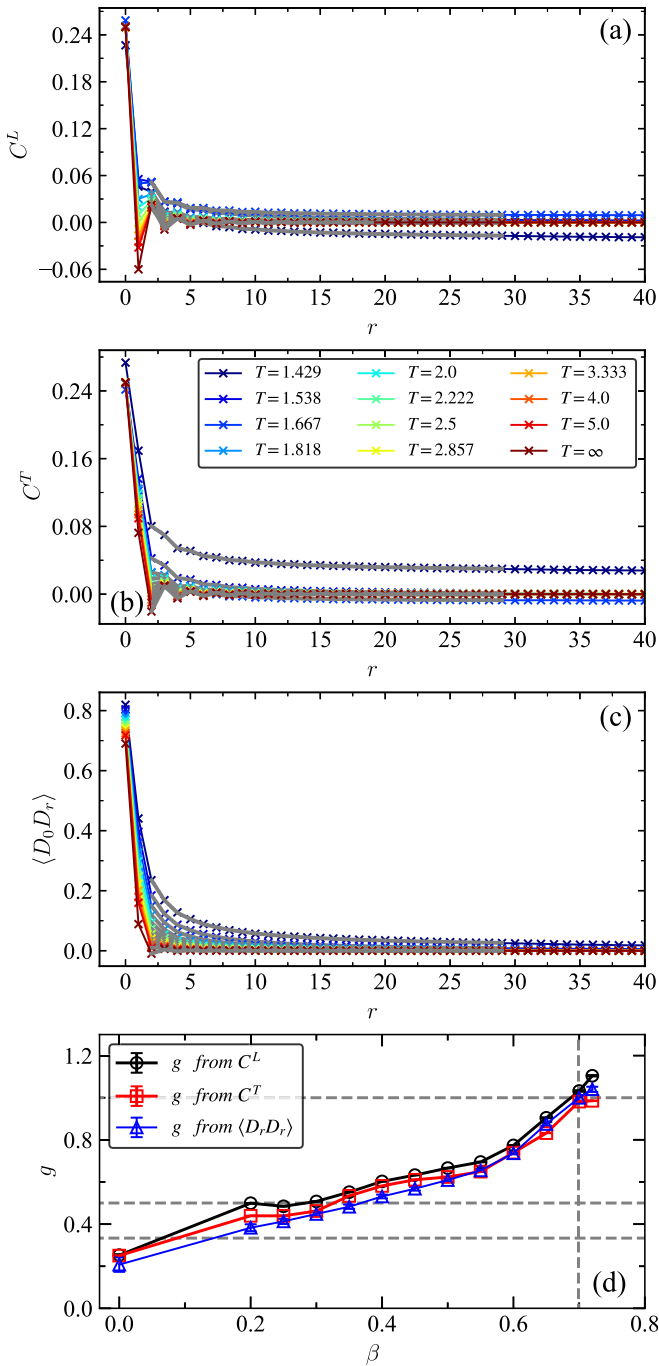


FIG. 8. The equal-time loop-segment correlation functions of (a) longitudinal loop-segment correlations C^L , (b) transverse correlations C^T , and (c) $\langle D_0 D_r \rangle$ in Eqs. (5), (6), and (8) in the main text. The system size here is $L = 256$. (d) The Coulomb gas constant g , as extracted from the various fits presented in previous panels, as a function of inverse temperature β .

(3) If the monomer is moving away from the dimer, growing a dimer in the process [Fig. 7(c)], it can, subsequently, destroy one of the two dimers connected to the node ahead or the monomer can just reverse its direction. Transition probabilities are chosen to satisfy detailed balance as described further below.

(4) We repeat steps (2) and (3) until the loop closes. If in the current configuration C' , the monomer M sees the

starting site S ahead of it [Fig. 7(d)], the loop can terminate and produce a fully packed configuration C with a Metropolis probability $p_{\text{term}} = \min(1, e^{\beta[E(C') - E(C)]})$. With probability $1 - p_{\text{term}}$, the M reverses the direction instead.

The probabilities p in steps (2) and (3) are chosen to satisfy detailed balance. As shown in Figs. 7(b) and 7(c) the current configuration C can transition into C'_0 with the monomer direction reversed or two other configurations $C'_{1,2}$. The probability of transition to $C'_{1,2}$ is given by

$$\frac{W_{1,2}}{Z - \min(W_1, W_2, W_0)}, \quad (\text{A1})$$

where $W_i = e^{-\beta E(C_i)}$, $Z = \sum_i W_i$.

The monomer correlator $M(r)$ is computed as the histogram of displacements between S and M . In the description of the algorithm above we have used the convention that the monomer sits at the center of the edge. We can instead choose to place the monomer M at some position $x \in [0, 1]$ on the dimer and associate an interaction energy between parallel full dimers and the “partial” dimers that is commensurate with x . We find that the choice of x adds a short-range correction that does not affect the scaling properties.

APPENDIX B: RAW DATA OF THE CORRELATION FUNCTIONS

We present in Figs. 8(a) and 8(b) the correlators $C^L(r)$ and $C^T(r)$ [measured in the $\mathbf{r} = (r, 0)$ direction] as well as the fits to the expressions (5) and (6). We furthermore present the correlator $\langle D_0 D_r \rangle$ associated to the order parameter in Fig. 8(c), which we fit to a single power law as its leading contribution should decay as $r^{-1/g}$. From these fits, we obtain estimates of g represented in the Fig. 8(d), which are in overall agreement to those obtained from fits to the adapted linear combinations of correlators presented in the main text (see Fig. 6), albeit with slightly larger fluctuations at high temperature.

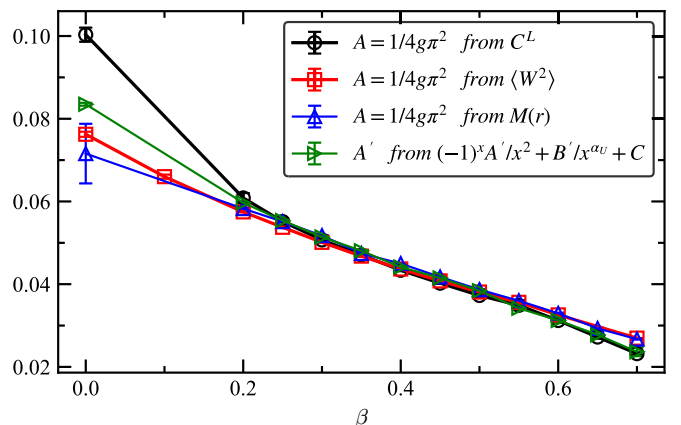


FIG. 9. Fits to obtain the coefficient A in Eq. (14) for the longitudinal loop-segment correlations C^L . Here we show the estimated values of A from $1/4g\pi^2$, where g is obtained in three ways: (black circular markers) from fitting to $(-1)^s A' / r^{\alpha s} + B' / r^{1/s} + C$, (red squares) from $\langle W^2 \rangle$, and (blue triangles Δ) from $M(r)$ (last two as described in Fig. 6). We also show A' obtained directly from the fit to $(-1)^s A' / r^2 + B' / r^{\alpha u} + C$. The four curves are consistent when β is large.

Aside from the evaluation of the Coulomb gas constant, we also comment in this Appendix on the evaluation of the amplitude [denoted A in Eqs. (5)–(7)] of the staggered part of loop-segment correlators, which is also expected to be universal (with g). We evaluate this amplitude from measurement of the longitudinal correlator $C^L(r)$ in four different ways (see Fig. 9): (i) assuming $A = 1/(4\pi^2g)$ where g is obtained from the scaling $(-1)^r A'/r^{\alpha_s} + B'/r^{1/g} +$

C ; (ii), (iii) $A = 1/(4\pi^2g)$ where g is from the winding number fluctuation (W^2) and the monomer correlator $M(r)$, respectively; (iv) A' obtained from the scaling form $(-1)^r A'/r^2 + B'/r^{\alpha_v} + C$.

We note an overall good agreement between all determinations of this amplitude, as soon as $\beta \geq 0.2$, albeit with some small discrepancy at $\beta = 0$. Overall these data are consistent with the prediction $A = 1/(4\pi^2g)$.

-
- [1] R. Moessner and S. L. Sondhi, *Phys. Rev. Lett.* **86**, 1881 (2001).
- [2] R. Moessner and S. L. Sondhi, *Phys. Rev. B* **63**, 224401 (2001).
- [3] S. T. Bramwell and M. J. P. Gingras, *Science* **294**, 1495 (2001).
- [4] G. Semeghini, H. Levine, A. Keesling, S. Ebadi, T. T. Wang, D. Bluvstein, R. Verresen, H. Pichler, M. Kalinowski, R. Samajdar, A. Omran, S. Sachdev, A. Vishwanath, M. Greiner, V. Vuletić, and M. D. Lukin, *Science* **374**, 1242 (2021).
- [5] R. Samajdar, W. W. Ho, H. Pichler, M. D. Lukin, and S. Sachdev, *Proc. Natl. Acad. Sci. USA* **118**, e2015785118 (2021).
- [6] S. Ebadi, T. T. Wang, H. Levine, A. Keesling, G. Semeghini, A. Omran, D. Bluvstein, R. Samajdar, H. Pichler, W. W. Ho, S. Choi, S. Sachdev, M. Greiner, V. Vuletić, and M. D. Lukin, *Nature (London)* **595**, 227 (2021).
- [7] Z. Yan, R. Samajdar, Y.-C. Wang, S. Sachdev, and Z. Y. Meng, *Nat. Commun.* **13**, 5799 (2022).
- [8] D. S. Rokhsar and S. A. Kivelson, *Phys. Rev. Lett.* **61**, 2376 (1988).
- [9] M. O. Blunt, J. C. Russell, M. d. C. Giménez-López, J. P. Garrahan, X. Lin, M. Schröder, N. R. Champness, and P. H. Beton, *Science* **322**, 1077 (2008).
- [10] I. A. Gruzberg, A. W. W. Ludwig, and N. Read, *Phys. Rev. Lett.* **82**, 4524 (1999).
- [11] N. Read and H. Saleur, *Nucl. Phys. B* **613**, 409 (2001).
- [12] P. Fendley, *Ann. Phys.* **323**, 3113 (2008).
- [13] A. Nahum, J. T. Chalker, P. Serna, M. Ortuño, and A. M. Somoza, *Phys. Rev. Lett.* **107**, 110601 (2011).
- [14] A. Nahum, J. T. Chalker, P. Serna, M. Ortuño, and A. M. Somoza, *Phys. Rev. X* **5**, 041048 (2015).
- [15] F. Alet, G. Misguich, V. Pasquier, R. Moessner, and J. L. Jacobsen, *Phys. Rev. Lett.* **97**, 030403 (2006).
- [16] S. Powell and J. T. Chalker, *Phys. Rev. Lett.* **101**, 155702 (2008).
- [17] D. Charrier, F. Alet, and P. Pujol, *Phys. Rev. Lett.* **101**, 167205 (2008).
- [18] S. Powell and J. T. Chalker, *Phys. Rev. B* **80**, 134413 (2009).
- [19] G. Chen, J. Gukelberger, S. Trebst, F. Alet, and L. Balents, *Phys. Rev. B* **80**, 045112 (2009).
- [20] G. J. Sreejith and S. Powell, *Phys. Rev. B* **92**, 184413 (2015).
- [21] G. J. Sreejith, S. Powell, and A. Nahum, *Phys. Rev. Lett.* **122**, 080601 (2019).
- [22] G. J. Sreejith and S. Powell, *Phys. Rev. B* **89**, 014404 (2014).
- [23] B. Nienhuis, in *Exact Methods in Low-dimensional Statistical Physics and Quantum Computing*, edited by J. Jacobsen, S. Ouvry, V. Pasquier, D. Serban, and L. F. Cugliandolo (Oxford University Press, Oxford, 2010), Chap. 6, pp. 159–195.
- [24] B. Nienhuis, in *Phase Transitions and Critical Phenomena*, edited by C. Domb and J. Lebowitz, Vol. 11 (Academic, New York, 1987), Chap. 1, pp. 1–53.
- [25] J. L. Jacobsen, Conformal field theory applied to loop models, in *Polygons, Polyominoes and Polycubes*, edited by A. J. Guttmann (Springer, Dordrecht, 2009), pp. 347–424.
- [26] A. Nahum, P. Serna, A. M. Somoza, and M. Ortuño, *Phys. Rev. B* **87**, 184204 (2013).
- [27] J. Kondev, J. de Gier, and B. Nienhuis, *J. Phys. A: Math. Gen.* **29**, 6489 (1996).
- [28] H. N. V. Temperley and E. H. Lieb, *Proc. R. Soc. London A* **322**, 251 (1971).
- [29] P. de Gennes, *Phys. Lett. A* **38**, 339 (1972).
- [30] J. L. Jacobsen, N. Read, and H. Saleur, *Phys. Rev. Lett.* **90**, 090601 (2003).
- [31] J. Cardy, *Ann. Phys.* **318**, 81 (2005), special Issue.
- [32] J. L. Jacobsen and F. Alet, *Phys. Rev. Lett.* **102**, 145702 (2009).
- [33] D. Schwandt, M. Mambrini, and D. Poilblanc, *Phys. Rev. B* **81**, 214413 (2010).
- [34] G. T. Barkema and M. E. J. Newman, *Phys. Rev. E* **57**, 1155 (1998).
- [35] F. Alet, Y. Ikhlef, J. L. Jacobsen, G. Misguich, and V. Pasquier, *Phys. Rev. E* **74**, 041124 (2006).
- [36] A. W. Sandvik and R. Moessner, *Phys. Rev. B* **73**, 144504 (2006).
- [37] O. F. Syljuåsen and A. W. Sandvik, *Phys. Rev. E* **66**, 046701 (2002).
- [38] O. F. Syljuåsen and M. B. Zvonarev, *Phys. Rev. E* **70**, 016118 (2004).
- [39] F. Alet and E. S. Sørensen, *Phys. Rev. E* **68**, 026702 (2003).
- [40] J. Kondev and C. L. Henley, *Nucl. Phys. B* **464**, 540 (1996).
- [41] R. Moessner, O. Tchernyshyov, and S. L. Sondhi, *J. Stat. Phys.* **116**, 755 (2004).
- [42] F. Alet, J. L. Jacobsen, G. Misguich, V. Pasquier, F. Mila, and M. Troyer, *Phys. Rev. Lett.* **94**, 235702 (2005).
- [43] S. Papanikolaou, E. Luijten, and E. Fradkin, *Phys. Rev. B* **76**, 134514 (2007).
- [44] S. Kundu and K. Damle, Flux fractionalization transition in two-dimensional dimer-loop models, [arXiv:2305.07012](https://arxiv.org/abs/2305.07012).
- [45] C. Castelnovo, C. Chamon, C. Mudry, and P. Pujol, *Ann. Phys.* **318**, 316 (2005).
- [46] S. Balasubramanian, V. Galitski, and A. Vishwanath, *Phys. Rev. B* **106**, 195127 (2022).
- [47] C. Castelnovo, C. Chamon, C. Mudry, and P. Pujol, *Ann. Phys.* **322**, 903 (2007).
- [48] L.-P. Henry and T. Roscilde, *Phys. Rev. Lett.* **113**, 027204 (2014).

- [49] N. Shannon, G. Misguich, and K. Penc, *Phys. Rev. B* **69**, 220403(R) (2004).
- [50] O. F. Syljuåsen and S. Chakravarty, *Phys. Rev. Lett.* **96**, 147004 (2006).
- [51] X. Plat, F. Alet, S. Capponi, and K. Totsuka, *Phys. Rev. B* **92**, 174402 (2015).
- [52] K. Roychowdhury, S. Bhattacharjee, and F. Pollmann, *Phys. Rev. B* **92**, 075141 (2015).
- [53] X. Ran, Z. Yan, Y.-C. Wang, J. Rong, Y. Qi, and Z. Y. Meng, *Phys. Rev. B* **107**, 125134 (2023).
- [54] Z. Yan, X. Ran, Y.-C. Wang, R. Samajdar, J. Rong, S. Sachdev, Y. Qi, and Z. Y. Meng, [arXiv:2205.04472](https://arxiv.org/abs/2205.04472).
- [55] B. Dabholkar, G. J. Sreejith, and F. Alet, *Phys. Rev. B* **106**, 205121 (2022).
- [56] Z. Yan, Z. Zhou, O. F. Syljuåsen, J. Zhang, T. Yuan, J. Lou, and Y. Chen, *Phys. Rev. B* **103**, 094421 (2021).
- [57] Z. Yan, Z. Y. Meng, D. A. Huse, and A. Chan, *Phys. Rev. B* **106**, L041115 (2022).
- [58] R. Verresen and A. Vishwanath, *Phys. Rev. X* **12**, 041029 (2022).
- [59] Z. Yan, Y.-C. Wang, N. Ma, Y. Qi, and Z. Y. Meng, *npj Quantum Mater.* **6**, 39 (2021).
- [60] F. Pollmann, J. J. Betouras, K. Shtengel, and P. Fulde, *Phys. Rev. B* **83**, 155117 (2011).
- [61] D. Banerjee, F.-J. Jiang, P. Widmer, and U.-J. Wiese, *J. Stat. Mech.: Theory Exp.* **2013**, P12010 (2013).
- [62] A. Browaeys and T. Lahaye, *Nat. Phys.* **16**, 132 (2020).
- [63] A. W. Glaetzle, M. Dalmonte, R. Nath, I. Rousochatzakis, R. Moessner, and P. Zoller, *Phys. Rev. X* **4**, 041037 (2014).
- [64] A. Celi, B. Vermersch, O. Viyuela, H. Pichler, M. D. Lukin, and P. Zoller, *Phys. Rev. X* **10**, 021057 (2020).
- [65] R. Verresen, M. D. Lukin, and A. Vishwanath, *Phys. Rev. X* **11**, 031005 (2021).
- [66] Z. Yan, Y.-C. Wang, R. Samajdar, S. Sachdev, and Z. Y. Meng, *Phys. Rev. Lett.* **130**, 206501 (2023).
- [67] E. H. Lieb and F. Y. Wu, in *Phase Transitions and Critical Phenomena: Exact Results*, edited by C. Domb and M. S. Green, Vol. 1 (Academic, London, 1972), Chap. 8, pp. 331–490.
- [68] E. H. Lieb, *Phys. Rev.* **162**, 162 (1967).
- [69] E. H. Lieb, *Phys. Rev. Lett.* **18**, 1046 (1967).
- [70] E. H. Lieb, *Phys. Rev. Lett.* **19**, 108 (1967).
- [71] B. Sutherland, *Phys. Rev. Lett.* **19**, 103 (1967).
- [72] E. H. Lieb, *Phys. Rev. Lett.* **18**, 692 (1967).
- [73] E. L. Pollock and D. M. Ceperley, *Phys. Rev. B* **36**, 8343 (1987).
- [74] P. Henelius, S. M. Girvin, and A. W. Sandvik, *Phys. Rev. B* **57**, 13382 (1998).
- [75] P. W. Leung, K. C. Chiu, and K. J. Runge, *Phys. Rev. B* **54**, 12938 (1996).
- [76] T. Paiva, R. R. dos Santos, R. T. Scalettar, and P. J. H. Denteneer, *Phys. Rev. B* **69**, 184501 (2004).
- [77] C. Chen, T. Yuan, Y. Qi, and Z. Y. Meng, *Phys. Rev. B* **103**, 165131 (2021).
- [78] N. C. Costa, T. Blommel, W.-T. Chiu, G. Batrouni, and R. T. Scalettar, *Phys. Rev. Lett.* **120**, 187003 (2018).
- [79] W. Jiang, Y. Liu, A. Klein, Y. Wang, K. Sun, A. V. Chubukov, and Z. Y. Meng, *Nat. Commun.* **13**, 2655 (2022).
- [80] R. Youngblood, J. D. Axe, and B. M. McCoy, *Phys. Rev. B* **21**, 5212 (1980).
- [81] B. Sutherland, *Phys. Lett. A* **26**, 532 (1968).
- [82] P. Falco, *Phys. Rev. E* **88**, 030103(R) (2013).
- [83] M. E. Fisher and J. Stephenson, *Phys. Rev.* **132**, 1411 (1963).
- [84] W. Krauth and R. Moessner, *Phys. Rev. B* **67**, 064503 (2003).
- [85] G. E. Andrews, R. J. Baxter, and P. J. Forrester, *J. Stat. Phys.* **35**, 193 (1984).
- [86] V. Pasquier, *Nucl. Phys. B* **285**, 162 (1987).
- [87] S. O. Warnaar, B. Nienhuis, and K. A. Seaton, *Phys. Rev. Lett.* **69**, 710 (1992).
- [88] H. W. J. Blöte and M. P. Nightingale, *Phys. Rev. B* **47**, 15046 (1993).
- [89] H. W. J. Blöte and B. Nienhuis, *Phys. Rev. Lett.* **72**, 1372 (1994).
- [90] J. Kondev and C. L. Henley, *Phys. Rev. B* **52**, 6628 (1995).
- [91] J. Kondev and C. L. Henley, *Phys. Rev. Lett.* **73**, 2786 (1994).
- [92] N. Wilkins and S. Powell, *Phys. Rev. B* **102**, 174431 (2020).
- [93] D. Sénéchal, in *Theoretical Methods for Strongly Correlated Electrons* (Springer, Berlin, 2004), pp. 139–186.
- [94] S. Lukyanov and V. Terras, *Nucl. Phys. B* **654**, 323 (2003).
- [95] J. V. José, L. P. Kadanoff, S. Kirkpatrick, and D. R. Nelson, *Phys. Rev. B* **16**, 1217 (1977).
- [96] D. J. Amit, Y. Y. Goldschmidt, and S. Grinstein, *J. Phys. A: Math. Gen.* **13**, 585 (1980).
- [97] J. M. Kosterlitz and D. J. Thouless, *J. Phys. C: Solid State Phys.* **6**, 1181 (1973).
- [98] J. M. Kosterlitz, *J. Phys. C: Solid State Phys.* **7**, 1046 (1974).
- [99] P. Ginsparg, *Nucl. Phys. B* **295**, 153 (1988).
- [100] P. Archambault, S. T. Bramwell, J.-Y. Fortin, P. C. W. Holdsworth, S. Peysson, and J.-F. Pinton, *J. Appl. Phys.* **83**, 7234 (1998).
- [101] J. Atchison, A. Bhullar, B. Norman, and D. Venus, *Phys. Rev. B* **99**, 125425 (2019).
- [102] S. V. Isakov and R. Moessner, *Phys. Rev. B* **68**, 104409 (2003).
- [103] T. Hikihara and A. Furusaki, *Phys. Rev. B* **58**, R583 (1998).
- [104] C. Castelnovo, C. Chamon, C. Mudry, and P. Pujol, *Phys. Rev. B* **73**, 144411 (2006).
- [105] Z. Yan, Y. Wu, C. Liu, O. F. Syljuåsen, J. Lou, and Y. Chen, *Phys. Rev. B* **99**, 165135 (2019).
- [106] Z. Yan, *Phys. Rev. B* **105**, 184432 (2022).
- [107] P. Scholl, M. Schuler, H. J. Williams, A. A. Eberharter, D. Barredo, K.-N. Schymik, V. Lienhard, L.-P. Henry, T. C. Lang, T. Lahaye, A. M. Läuchli, and A. Browaeys, *Nature (London)* **595**, 233 (2021).